Water Vapor Retrieval Using Commercial Microwave Links Based on the LSTM Network

Kang Pu, Xichuan Liu, Lei Liu, and Taichang Gao

***Abstract*—In this article, a water vapor density inversion model based on the long short-term memory network is proposed for E-band commercial microwave links (CMLs). A full-duplex E-band microwave link located in Prague (two sublinks with frequencies of 73.5 and 83.5 GHz, both vertically polarized) was used to verify the performance of the model. The results show that the model inversion results are in good agreement with the water vapor density calculated by temperature and humidity sensors. Compared with previous water vapor inversion methods based on CMLs, this model has a higher temporal resolution and can realize real-time monitoring.**

***Index Terms*—E-band, humidity monitoring, wireless communication network.**

I. Introduction

WATER vapor is the only atmospheric component that can undergo three phase changes under normal atmospheric conditions, and its content varies greatly in space (the difference between the wettest and the driest regions can reach up to five orders of magnitude) [1]. Water vapor diffusion and transport are important parts of the water cycle and are crucial to the formation of various weather processes [2], [3]. In particular, the occurrence of extreme rainfall is closely related to specific water vapor transport paths [4], [5]. Approximately 70% of precipitation comes from atmospheric water vapor in extratropical cyclones [6]. Additionally, the accuracy of numerical weather prediction models depends largely on the accurate detection of water vapor [7]. Therefore, the accurate monitoring of water vapor is beneficial to the prediction of disastrous weather events. In addition, water vapor, as a special greenhouse gas, has a thermal feedback effect that exacerbates the greenhouse effect [8]. Furthermore, changes in the radiation characteristics of clouds due to changes in water vapor also have significant effects on climate models [9].

A variety of humidity measurement methods based on different platforms and detection principles have been proposed in the last century [10]–[12]. Single-point humidity sensors are now widely deployed at weather stations around the world [13]. Although these sensors are sufficiently accurate, their spatial representation is obviously unable to meet current meteorological monitoring requirements. Radiosondes with humidity sensors are generally used to detect humidity with high precision and can provide humidity profiles with a high vertical spatial resolution [14]. However, the cost of a radiosonde is high because it can be used only once, and its temporal resolution and horizontal spatial resolution are very low. Space-borne infrared or microwave radiometers are capable of sensing the humidity distribution across the globe [15], but they do not perform well on land due to surface temperatures. Moreover, the surface may be obscured by clouds, making it difficult to monitor the humidity distribution in the lower atmosphere. Ground-based microwave radiometers [16] overcome these problems, but these instruments need to be recalibrated during operation and may be affected by surface water adhesion.

In recent years, research has been conducted on the use of commercial microwave links (CMLs) for the monitoring of meteorological elements [17]–[19], the main principle of which is that the attenuation of microwave signals recorded by CML is affected by atmospheric properties along the path. Due to the near-surface characteristics, high temporal resolution and wide distribution of readily available equipment, CMLs are a very effective supplement to traditional methods used to monitor atmospheric properties [20]. The first focus of research in this field is to invert the path-averaged rain rate by a rain attenuation model [21], [22], and then to extend the results to the reconstruction of rainfall fields [23], [24], the inversion of raindrop size distributions [25], [26], and the classification of precipitation types [27], [28]. In addition, David *et al.* [29] revealed the great potential of CMLs for fog monitoring and carried out simulation experiments at frequencies of 20, 38, and 80 GHz. Moreover, David *et al.* [30] proposed that the near-surface temperature and atmospheric pollutants could be detected with CMLs, and an NO_x episode, a PM10 episode, and a fog episode were correspondingly analyzed. Furthermore, David *et al.* [31] presented a new method for water vapor detection using CMLs near the water vapor absorption band at a frequency of 22 GHz. An effort was also made to reconstruct the water vapor field at frequencies of 22 and 86 GHz [32].

The above CML-based water vapor inversion method requires that a reference received signal level (RSL) be determined in advance. The reference RSL is usually set to the median RSL during a few weeks. This approach creates several problems. First, the reference RSL needs to be constantly updated every

Manuscript received August 7, 2020; revised December 5, 2020 and March 11, 2021; accepted April 3, 2021. Date of publication April 13, 2021; date of current version May 6, 2021. This work was supported in part by the National Natural Science Foundation of China under Grant 41975030, Grant 41505135, and Grant 41475020. *(Corresponding author: Xichuan Liu.)*

The authors are with the College of Meteorology and Oceanography, National University of Defense Technology, Changsha 410003, China (e-mail: pkpk12321pkpk@gmail.com; liuxc2012@hotmail.com; liuleidll@gmail.com; 2009gaotc@gmail.com).

Digital Object Identifier 10.1109/JSTARS.2021.3073013

few weeks, and the water vapor cannot be monitored in real time. In addition, unlike rain-induced attenuation, the concept of water vapor attenuation obtained here by subtracting the reference RSL is not clear and may be more appropriately referred to as the change in water vapor attenuation. Moreover, the temporal resolution is only 1 day since only one RSL value is provided at a fixed time of day; hence, it is obviously difficult to achieve the high temporal resolution needed for water vapor monitoring. According to the above paper, this setting is due to the configuration of the system, and the data sampling interval can be shortened. However, no inversion results with a higher temporal resolution have been evaluated. Therefore, it is worth investigating how to obtain the water vapor content in real time with a high temporal resolution using CMLs.

With the continuous development of 5G networks, more high-frequency CMLs [e.g., E-bands (71–76 and 81–86 GHz), which are defined by the recommended frequency band of operation of WR12 waveguides] have been deployed around the world to increase transmission capacity and reduce transmission latency [33]. Fencl *et al.* [34] proved that the observed gas attenuation and theoretical gas attenuation have a high correlation for E-band CMLs and indicated that the inversion of water vapor is possible for E-band links spanning several kilometers in length during the dry period. Based on the above, this article proposes a real-time water vapor density monitoring method with a high temporal resolution based on the long short-term memory (LSTM) network using E-band CMLs. The rest of this article is arranged as follows: The next section describes the principle of the water vapor inversion with E-band CMLs and the open-source data used in the study. Section III analyzes the relationship between the water vapor density and feature variables extracted from the total attenuation of E-band CMLs. The water vapor inversion model based on the LSTM network is introduced in Section IV. Sections V and VI evaluate the performance and error sources, respectively. Section VII tries another variant of the network and compares its results with those of the LSTM network. Finally, the conclusion is presented in Section VIII.

II. Principle and Data

For a terrestrial microwave link, the total signal power loss (dB) along the link can be calculated as follows:

$$A_{\text{total}} = \text{TSL} + G_T + G_R - \text{RSL} \tag{1}$$

where TSL (dBm) and RSL (dBm) are the transmitted and RSLs, respectively, and G_T (dBm) and G_R (dBm) are the antenna gain at the transmitting and receiving terminals, respectively. A_{total} is mainly composed of the following parts:

$$A_{\text{total}} = A_{\text{space}} + A_{\text{dry}} + A_{\text{vapor}} + A_{\text{hydro}} + A_{\text{wa}} + A_{\text{other}} \tag{2}$$

where A_{space} (dB) refers to the free space attenuation; A_{dry} (dB) refers to the dry air attenuation (for millimeter-wave bands, the main absorbing gas is oxygen); A_{vapor} (dB) refers to the water vapor attenuation; A_{hydro} (dB) refers to the attenuation caused by hydrometeors, such as raindrops, snowflakes, and fog droplets; A_{wa} (dB) refers to the wet antenna attenuation; and A_{other} (dB) refers to the additional attenuation caused by the instrument itself, for example, corresponding to the stability and quantitative resolution of the equipment. For fixed links, A_{space}, A_{dry}, and A_{other} can be regarded as constants in the range of normal surface temperatures and pressure changes (except near the oxygen absorption band of 60 GHz, as shown in Fig. 1). In addition, the influences of A_{hydro} and A_{wa} can be ignored during the dry period. Therefore, water vapor attenuation during the dry period can be expressed as

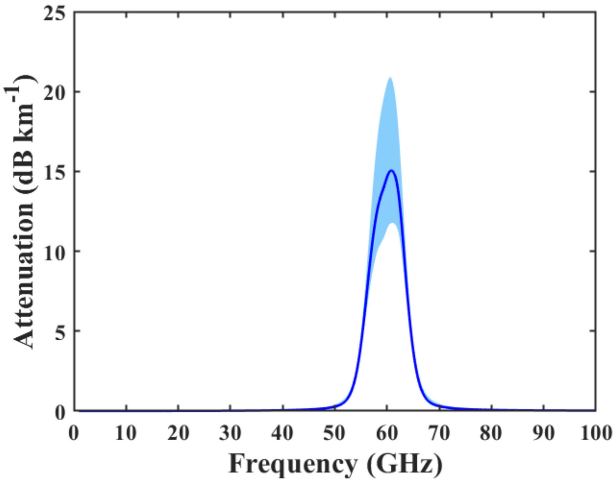

Fig. 1. Dry air attenuation at temperatures ranging from −20 to 40 °C and atmospheric pressures ranging from 950 to 1060 hPa (according to the ITU-R P.676-10 recommendation) for frequencies from 1 to 100 GHz. Solid line refers to the dry air attenuation when temperature is 15 °C and atmospheric pressure is 1013.25 hPa. Blue-shaded region refers to the range of dry air attenuation when temperature is ranging from −20 to 40 °C and pressure is ranging from 950 to 1060 hPa.

$$A_{\text{vapor}} = A_{\text{total}} - \text{constant (if dry period)} \tag{3}$$

where constant stands for a constant. According to (3), during the dry period, the fluctuation of A_{total} is actually caused by a change in the water vapor content. However, due to the influence of noise, the appropriate bands need to be chosen to extract the water vapor attenuation from A_{total}. As shown in Fig. 2, the attenuation value of water vapor is far less than that of dry air (less than one-tenth) at approximately 60 GHz. Therefore, the inversion of water vapor at approximately 60 GHz will be affected immensely by noise, and thus, unsatisfactory results will be obtained. Outside this frequency range, when the frequency is greater than 70 GHz, the water vapor attenuation will obviously exceed the dry air attenuation; this is the appropriate frequency band for the theoretical inversion of the water vapor content. The same occurs at frequencies below 50 GHz, especially in the water vapor absorption band near 22 GHz. In addition, the water vapor attenuation at frequencies greater than 70 GHz is relatively more sensitive to the water vapor density than that near 22 GHz (the value of the attenuation caused by the same water vapor density change varies more at the former), which means that frequencies greater than 70 GHz are more suitable for water vapor inversion than those near 22 GHz.

The method employed to invert the water vapor density in this article is based on a bidirectional E-band microwave link. The

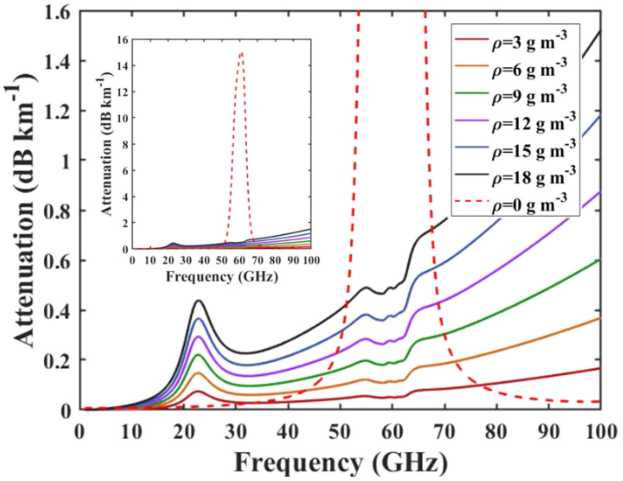

Fig. 2. Water vapor attenuation at different water vapor densities for frequencies from 1 to 100 GHz (the dashed line represents dry air attenuation at a temperature of 15 °C and an atmospheric pressure of 1013.25 hPa).

measured data are from the open-source data shared by Fencl *et al.* [34]. These links are located in the southeastern suburb of Prague, the capital of the Czech Republic. There are a total of six E-band links of different lengths with full-duplex configurations; we selected one of these links, ID 1147_1148. The link length is 4.866 km. The sampling time of both the receiving terminal and the transmitting terminal is approximately 10 s, and the quantization resolution is 0.1 dB. The two terminals of the link transmit and receive vertically polarized microwave signals at 73.5 GHz (Link 1148) and 83.5 GHz (Link 1147), respectively. Both the RSL and the TSL are recorded by custom software. For the convenience of processing, the sampled data were integrated to a 1-min temporal resolution. The data were recorded from August 20 to December 16, 2018 (119 days), with 37 days of rain. The dry periods between rainy periods were extracted for the inversion of water vapor. Dry events with a duration of less than 1440 min were excluded, and the data of the first 5 h of each dry period event were deleted to prevent the influence of the wet antenna effect that remains after rain. After the above processing, a total of 21 dry period events were obtained, as shown in Table I.

In addition, one end of the link is equipped with humidity and temperature sensors, whose temporal resolution is 5 min. Since the humidity sensor records the relative humidity RH, it needs to be converted into the water vapor density ρ (g m^{-3}) through the following equation:

$$\rho = e/(R_v \cdot (t + 273.15)) = (\mathrm{RH} \cdot E)/(R_v \cdot (t + 273.15)) \tag{4}$$

where e (Pa) refers to the water vapor pressure; R_v [J/(kg·K)] refers to the specific gas constant of water vapor; t (°C) refers to the temperature in Celsius; and E (Pa) refers to the saturation water vapor pressure, which can be obtained by Magnus's empirical formula [35]:

$$E = E_0 10^{\frac{at}{b+t}} \tag{5}$$

where $E_0 = 6.11$ hPa, $a = 7.5$ °C, and $b = 237.3$ °C.

TABLE I
TWENTY-ONE DRY PERIOD EVENTS

Number	Period (MMDD HH:mm)
1	0820 05:00 ~ 0823 23:00
2	0824 15:00 ~ 0831 22:00
3	0903 12:00 ~ 0907 09:00
4	0907 15:00 ~ 091312:00
5	0914 09:00 ~ 0915 05:00
6	0915 12:00 ~ 0921 18:00
7	0922 05:00 ~ 0923 10:00
8	1002 02:00 ~ 1003 07:00
9	1003 15:00 ~ 1022 18:00
10	1023 00:00 ~ 1024 04:00
11	1024 19:00 ~ 1027 04:00
12	1030 11:00 ~ 1102 19:00
13	1103 22:00 ~ 1119 08:00
14	1119 14:00 ~ 1120 13:00
15	1121 18:00 ~ 1124 08:00
16	1125 12:00 ~ 1128 09:00
17	1128 15:00 ~ 1201 12:00
18	1204 14:00 ~ 1208 02:00
19	1208 08:00 ~ 1209 17:00
20	1210 04:00 ~ 1211 09:00
21	1212 17:00 ~ 1216 00:00

III. ANALYSIS OF FEATURES

According to (3), the change in the water vapor attenuation during the dry period is actually approximately equal to the change in the total attenuation. Therefore, information on the water vapor content is contained in the total attenuation. Setting the time step Δt as 5 min, dry period event i (Event$_i$) can be seen as numerous small time series of 5 min each:

$$\begin{gathered}\mathrm{Event}_i = \{\mathrm{series}_{i,1}, \mathrm{series}_{i,2}, \ldots, \mathrm{series}_{i,k}, \ldots, \mathrm{series}_{i,n}\} \\ \mathrm{series}_{i,k} = \{A_{\mathrm{total},(i,5k-4)}, A_{\mathrm{total},(i,5k-3)}, \ldots, A_{\mathrm{total},(i,5k)}\} \\ i = 1, \ldots, 21; k = 1, 2, \ldots, n; n = [\mathrm{number}(\mathrm{Event}_i)/5]\end{gathered} \tag{6}$$

where number(Event$_i$) refers to the number of minutes of Event$_i$. For series$_{i,k}$, the following characteristics can be extracted:

$$\begin{aligned}\mathrm{Median}_{i,k} &= \mathrm{MEDIAN}(\mathrm{series}_{i,k}) \\ \mathrm{Std}_{i,k} &= \mathrm{STD}(\mathrm{series}_{i,k}) \\ \mathrm{Max}_{i,k} &= \mathrm{MAX}(\mathrm{series}_{i,k}) \\ \mathrm{Min}_{i,k} &= \mathrm{MIN}(\mathrm{series}_{i,k}) \\ \mathrm{Slope}_{i,k} &= \mathrm{SLOPE}(\mathrm{series}_{i,k})\end{aligned} \tag{7}$$

where MEDIAN, STD, MAX, MIN, and SLOPE refer to the median function, standard deviation function, maximum function, minimum function, and slope function (obtained by first-order least square fitting), respectively. In addition, since water vapor has a daily variation, the daily time label (Timelabel$_{i,k}$) corresponding to series$_{i,k}$ can also be defined as a feature variable (for a time step of 5 min, the time label of a day can range from 1 to 288). Fig. 3 shows 2-D scatterplots of the water vapor density versus the several feature variables mentioned above for both sublinks. It can be seen from the figure that Median [Fig. 3 (a) and (b)], Max [Fig. 3 (e) and (f)], and Min [Fig. 3 (g) and (h)] have obvious positive correlations with ρ for both 73.5 and 83.5 GHz, so they are all helpful features in the water vapor density inversion. In addition, although the scatters are more dispersive [Fig. 3(m)], ρ fluctuates with Timelabel in the intermediate

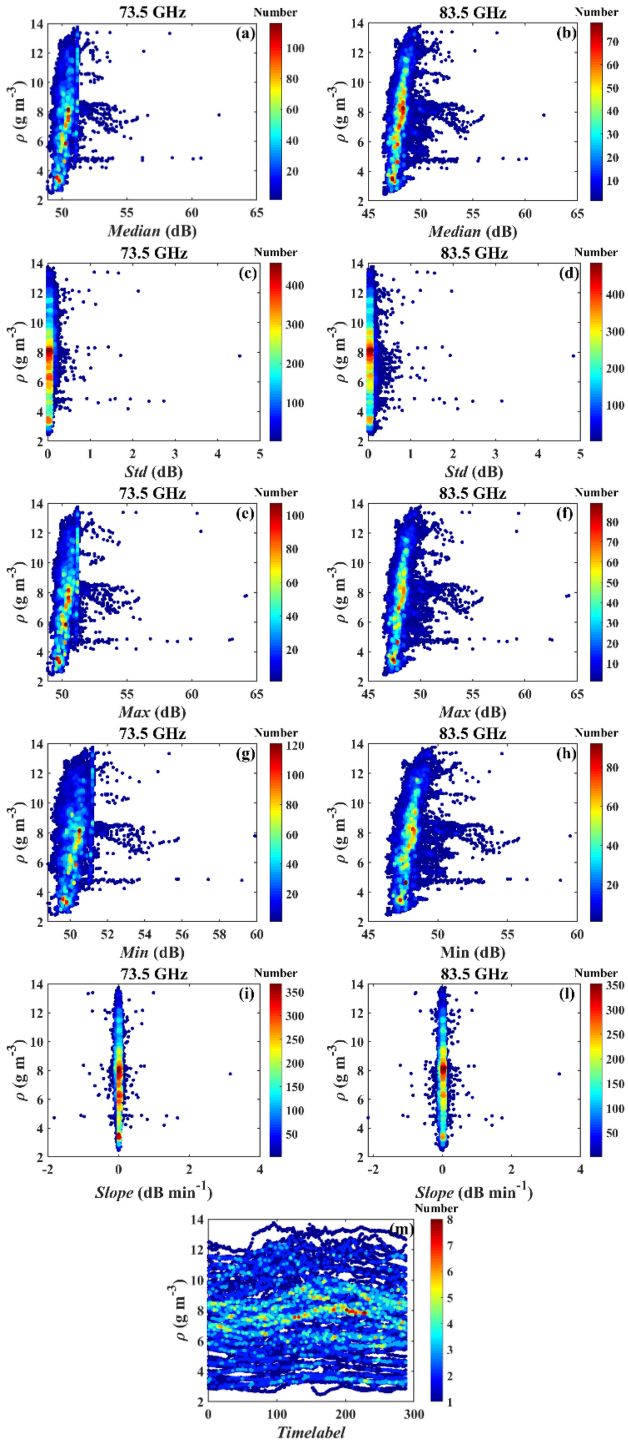

Fig. 3. 2-D scatterplots of six statistical features [(a) and (b) median (dB), (c) and (d) standard deviation, (e) and (f) maximum, (g) and (h) minimum, (i) and (l) slope, and (m) time label)] and water vapor density ρ (g m^{-3}) with a 5-min time step for both 73.5 and 82.75 GHz.

region, which verifies the diurnal variation characteristics of water vapor. Furthermore, Std [Fig. 3 (c) and (d)] and Slope [Fig. 3 (i) and (l)] are not very sensitive to changes in ρ, so they seem to be of little help in the retrieval model with no memory function.

IV. Model Based on the LSTM Network

Unlike the high temporal variability of the rain intensity, the water vapor density changes relatively slowly. Correspondingly, different from the rapidity of the change in rain-induced attenuation, the change in water vapor attenuation also occurs relatively slowly. The water vapor density at the previous moment must affect the water vapor density at the current moment. Therefore, a memory module must be introduced into the water vapor density inversion model. According to Section III, the water vapor density is correlated with Median, Max, Min, and Timelabel, while the correlations with Std and Slope are not obvious. However, for the model with memory, the changes in Slope and Std over time can reflect the trend and fluctuation of the water vapor density over time, so we also take Slope and Std as features. For dual-frequency link 1147_1148, the feature extracted at the kth time step of the ith dry period event is as follows:

$$\mathrm{Feature}_{i,k} = [\mathrm{Feature}_{i,k,73.5}, \mathrm{Feature}_{i,k,83.5}, \mathrm{Timelabel}_{i,k}] \tag{8}$$

where

$$\mathrm{Feature}_{i,k,73.5} = [\mathrm{Median}_{i,k,73.5}, \mathrm{Std}_{i,k,73.5}, \ldots \mathrm{Max}_{i,k,73.5}, \mathrm{Min}_{i,k,73.5}, \mathrm{Slope}_{i,k,73.5}] \tag{9}$$

$$\mathrm{Feature}_{i,k,83.5} = [\mathrm{Median}_{i,k,83.5}, \mathrm{Std}_{i,k,83.5}, \ldots \mathrm{Max}_{i,k,83.5}, \mathrm{Min}_{i,k,83.5}, \mathrm{Slope}_{i,k,83.5}]. \tag{10}$$

A model with a memory mechanism, namely, the Hopfield network, was previously proposed [36]. On this basis, a recurrent neural network (RNN) that can process serial data was developed [37]. Through the feedback connection of internal neurons, RNNs can handle time series or text series problems well [38]. However, RNNs do not have long-term memory, and gradient vanishing may occur in the RNN training process, which limits the performance of the model. The LSTM network, an improved model, solves these problems by introducing gate functions [39]. As shown in Fig. 4, each memory cell consists of three gates. The first is the forget gate, which realizes the selective inheritance of past memories:

$$F_k = \sigma(W_F[\rho_{i,k-1}, \mathrm{Feature}_{i,k}] + b_F) \tag{11}$$

where $\rho_{i,k-1}$ ($\mathrm{Feature}_{i,k}$) corresponds to the hidden state (input feature) of the previous (current) time step; W_F and b_F are the weight and bias of the forget gate, respectively; and σ is the sigmoid function with an output from 0 to 1, which is used to filter the cell state C_{k-1} of the previous time step. The second gate is the input gate that determines which parts of the current information are stored in the memory cell:

$$I_k = \sigma(W_I[\rho_{i,k-1}, \mathrm{Feature}_{i,k}] + b_I) \tag{12}$$

$$\tilde{C}_k = \tanh(W_C[\rho_{i,k-1}, \mathrm{Feature}_{i,k}] + b_C) \tag{13}$$

where W_I (W_C) and b_I (b_C) are the weight and bias of the input gate, respectively. Thus, the current state of the memory cell is updated as follows:

$$C_k = F_k * C_{k-1} + I_k * \tilde{C}_k\,. \tag{14}$$

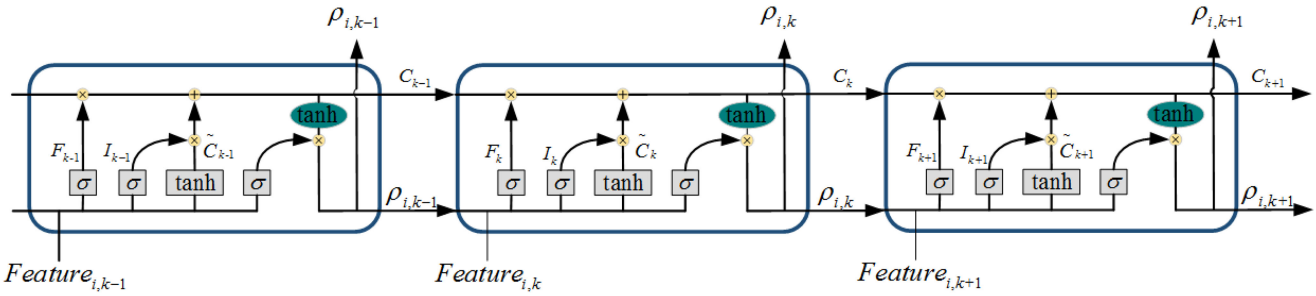

Fig. 4. Schematic diagram of the water vapor density inversion model based on the LSTM network. Three rectangles represent the memory cells of the previous, current, and later time steps. Arrows represent the flow of data.

Finally, the output gate outputs the current hidden state based on the current cell state and input information:

$$\rho_{i,k} = \sigma(W_O[\rho_{i,k-1}, \text{Feature}_{i,k}] + b_O) * \tanh(C_k) \quad (15)$$

where W_O and b_O are the weight and bias of the output gate, respectively. Dry period events 6 and 9 were selected as the test set, and the other events were selected as the training set. The network contains an LSTM layer with 400 hidden units, a full connection layer of size 100, and a discard layer with a probability of 0.5.

V. Performance Evaluation

To evaluate the performance of the water vapor density inversion model based on the LSTM network, some evaluation indexes need to be calculated. Here, the Pearson correlation coefficient (dimensionless), root-mean-square error (g m^{-3}), mean bias (g m^{-3}), and relative absolute bias (dimensionless) are used:

$$\text{PCC} = \frac{\sum_{k=1}^{n}(\rho_{\text{lstm},k} - \bar{\rho}_{\text{lstm}})(\rho_{\text{sensor},k} - \bar{\rho}_{\text{sensor}})}{(\sum_{k=1}^{n}(\rho_{\text{lstm},k} - \bar{\rho}_{\text{lstm}})^2)^{1/2}(\sum_{k=1}^{n}(\rho_{\text{sensor},k} - \bar{\rho}_{\text{sensor}})^2)^{1/2}} \quad (16)$$

$$\text{RMSE} = \left(\frac{\sum_{k=1}^{n}(\rho_{\text{lstm},k} - \rho_{\text{sensor},k})^2}{n}\right)^{1/2} \quad (17)$$

$$\text{MB} = \frac{\sum_{k=1}^{n}(\rho_{\text{lstm},k} - \rho_{\text{sensor},k})}{n} \quad (18)$$

$$\text{RAB} = \frac{1}{n}\sum_{k=1}^{n}\left|\frac{\rho_{\text{lstm},k} - \rho_{\text{sensor},k}}{\rho_{\text{sensor},k}}\right|. \quad (19)$$

Fig. 5 shows the water vapor inversion results in two dry period events as the test set. For event 6, except for a few areas, the water vapor density ρ_{lstm} obtained by the inversion model based on the LSTM network has good consistency with the water vapor density ρ_{sensor} calculated from humidity and temperature sensor measurements (PCC = 0.91), which is slightly overestimated (RMSE = 0.73 g m^{-3}, MB = 0.23 g m^{-3}, RAB = 5.49%) (as shown in Table II). For event 9 (time span of 19 days), the water vapor density inversion results are worse (PCC = 0.79, RMSE = 0.90 g m^{-3}, MB = 0.40 g m^{-3}, RAB = 8.22%) (as shown in Table II). For some uplift areas, although the inversion model may overestimate the water vapor density, the overall water vapor density trend can still be tracked effectively. This result corresponds to the analysis of Fencl *et al.* [34], who suggest that the theoretical and observed gas attenuations are more consistent in summer than in autumn (the possible reason is that water vapor is more abundant in summer).

TABLE II
Pearson Correlation Coefficient (PCC), Root-Mean-Square Error (RMSE), and Mean Bias (ME) of ρ_{LSTM} Relative to ρ_{SENSOR}

Period	PCC	RMSE (g m^{-3})	MB (g m^{-3})	RAB
15th Sep to 21st Sep	0.9065	0.7338	0.2259	5.49%
3rd Oct to 22nd Oct	0.7853	0.8988	0.3966	8.22%

VI. Error Source

According to Section V, the water vapor inversion model in this article contains some sources of error. First, the measurement error of the humidity sensor itself may lead to some deviations in the observed water vapor density. Additionally, since the humidity sensor is a single-point instrument, whether it can represent the path-averaged water vapor content remains to be verified. In addition, the stability of the microwave transmitter and receiver will also affect the evaluation. The performance of the device can be altered by mechanical vibrations (strong winds) or by changes in temperature and humidity. Moreover, the quantification error cannot be ignored. For the links used in this article (quantization level of 0.1 dB and path length of 4.866 km), the uncertainties range from 0.30 to 0.74 g m^{-3} and from 0.27 to 0.59 g m^{-3} for 73.5 and 83.5 GHz, respectively. Increasing the link length will reduce the quantization error. Furthermore, although we excluded rainy periods and the subsequent 5 h to prevent the wet antenna effect, the influences of fog and dew are difficult to eliminate without the support of other observational data.

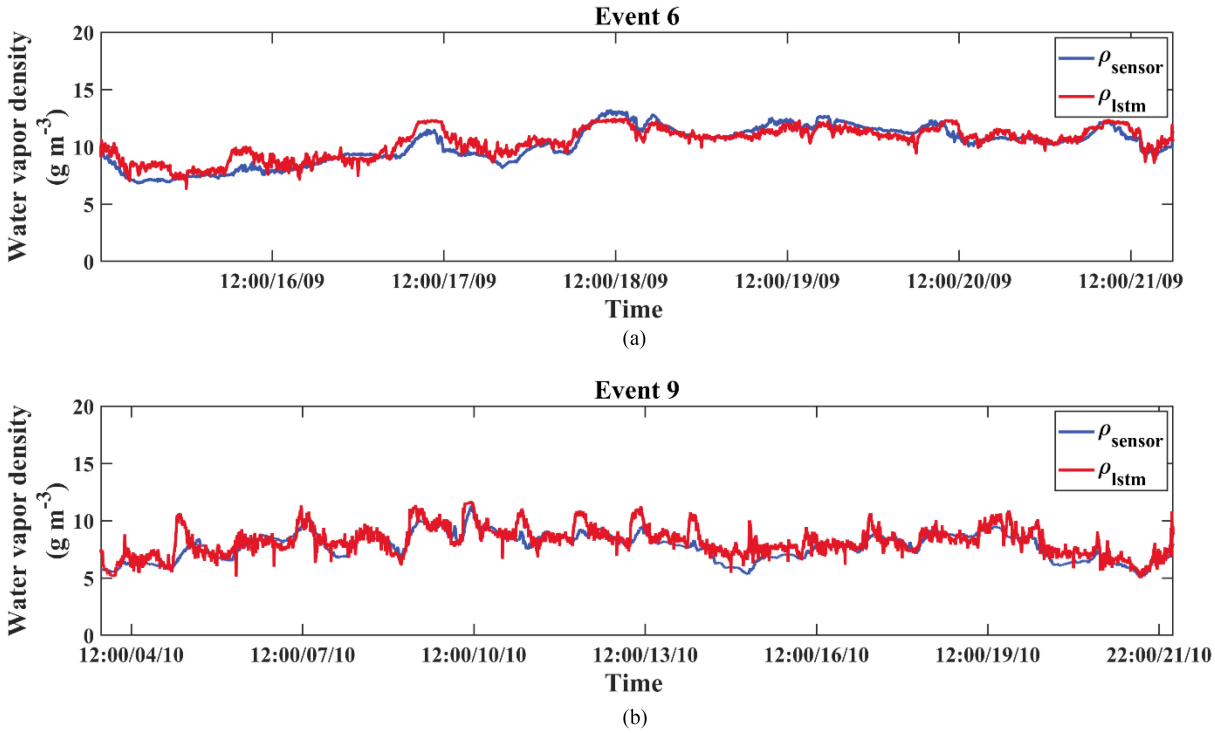

Fig. 5. Two dry periods [from 12:00 on September 15th to 18:00 on September 21th (a) and from 15:00 on October 3rd to 18:00 on October 22nd (b)]. Blue line represents the change in the water vapor density calculated from humidity and temperature sensor measurements with time, and the red line represents the change in the water vapor density obtained by the inversion based on the LSTM network with time in this study.

VII. Discussion

By determining the attenuation baseline (usually set to the median RSL during a few weeks), David *et al.* [31] used two microwave links with frequency points around 22 GHz (respectively, located in northern Israel and central Israel) to invert the change of water vapor density during about one month. The two link measurement results are PCC = 0.9, RMSE = 1.8 gm^{-3}, and PCC = 0.82, RMSE = 3.4 $\mathrm{g\ m}^{-3}$, respectively. Relatively, the effect of water vapor density inversion using E-band microwave link based on LSTM network in this article may be better. In addition, the inversion method of water vapor density using the median RSL value of several weeks as the reference level cannot deal with these short time events. In this respect, the method proposed in this article has obvious advantages, which can obtain water vapor density information at high resolution in real time.

Due to the limited data available, this article can only use dry period events as shown in Table I to build and validate the model, which means that the model only performs well in late summer to early winter in mid-latitude regions, while other conditions have yet to be tested. In the future, with the continuous accumulation of experimental data (in addition to a longer period of time, sample collection experiments under different climate, terrain, and weather conditions will also be carried out), the training cost of inversion model will also increase continuously. In addition to using high-performance computers to solve computational problems, a reasonable improved algorithm is also helpful for the further popularization of this method. A variant of LSTM: gated recurrent unit (GRU) [40] seems to be beneficial. By combining

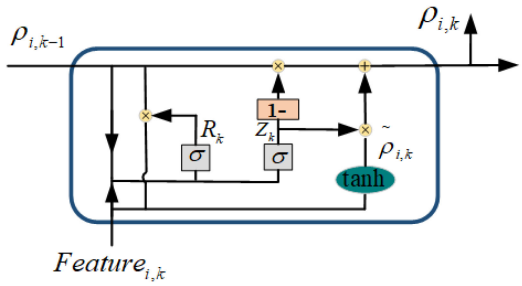

Fig. 6. Schematic diagram of single memory cells for the water vapor density inversion model based on GRU network. Arrows represent the flow of data.

the forget gate and the input gate into a single update gate and some other changes, the final model is similar to LSTM, but with one-third fewer parameters, significantly faster training and less over-fitting. Structurally, the GRU has only two gates (reset gate and update gate). Fig. 6 shows the schematic diagram of single memory cells for the water vapor density inversion model based on GRU network. The reset gate is used to determine what information from the past needs to be forgotten:

$$R_k = \sigma(W_R[\rho_{i,k-1}, \mathrm{Feature}_{i,k}] + b_R) \tag{20}$$

where W_R and b_R are the weight and bias of the reset gate, respectively. The update gate controls the extent to which previous hidden state is carried into the current hidden state

$$Z_k = \sigma(W_Z[\rho_{i,k-1}, \mathrm{Feature}_{i,k}] + b_Z) \tag{21}$$

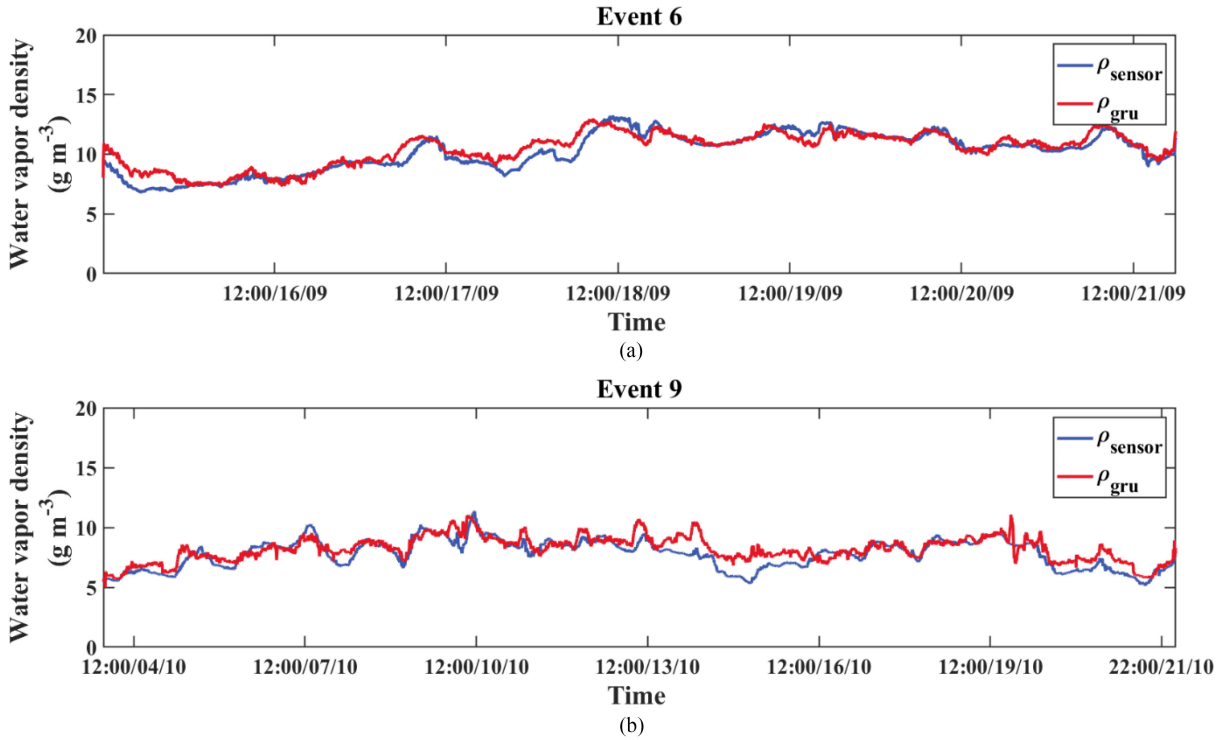

Fig. 7. Two dry periods [from 12:00 on September 15th to 18:00 on September 21th (a) and from 15:00 on October 3rd to 18:00 on October 22nd (b)]. Blue line represents the change in the water vapor density measured by the sensor with time, and the red line represents the change in the water vapor density obtained by the inversion based on the GRU network with time in this study.

TABLE III
PEARSON CORRELATION COEFFICIENT (PCC), ROOT-MEAN-SQUARE ERROR (RMSE), AND MEAN BIAS (ME) OF ρ_{GRU} RELATIVE TO ρ_{SENSOR}

Period	PCC	RMSE (g m^{-3})	MB (g m^{-3})	RAB
15th Sep to 21st Sep	0.9215	0.6831	0.2583	4.61%
3rd Oct to 22nd Oct	0.8316	0.7786	0.3867	7.11%

where W_Z and b_z are the weight and bias of the update gate, respectively. Instead of using cell states, the GRU uses hidden states to transmit information:

$$\rho_{i,k} = \tilde{\rho}_{i,k} * Z_k + \rho_{i,k-1} * (1 - Z_k) \tag{22}$$

where $\tilde{\rho}_{i,k} = \tanh(W_\rho[\rho_{i,k-1} * R_k, \text{Feature}_{i,k}] + b_\rho)$, W_ρ and b_ρ are the weight and bias of the GRU unit.

In order to compare the results of water vapor density inversion by LSTM network and GRU network, single memory cell as shown in Fig. 6 were used to replace the memory cells as shown in Fig. 4, and other network parameters were set unchanged. In addition, the data used in the training and testing of the water vapor density inversion model based on GRU network is the same as that based on LSTM network. Table III shows the test results. Through the analysis, it can be seen that the GRU network and LSTM network have basically the same effect in the inversion of water vapor density. In addition, the water vapor density tracking curves of the two test dry period events based on the GRU network in Fig. 7 also show a good agreement with the measured results of humidity sensor. Furthermore, the water vapor density tracking curve based on GRU network is smoother than that based on LSTM, which may be corresponding to the less over-fitting of GRU network mentioned above. In fact, LSTM and GRU networks are not clearly superior to each other in terms of performance. LSTM networks may perform slightly better when the volume of data is very high. The GRU has fewer parameters, trains faster, and requires less data. However, considering the small fluctuation of the values of evaluation indexes for each training result, this difference is not very significant.

VIII. CONCLUSION

In view of the existing problems facing the inversion of water vapor based on CMLs, this article proposes a water vapor density inversion model based on the LSTM network using dual-frequency E-band CMLs. The proposed model has the advantages of a high temporal resolution and real-time monitoring, which has the potential to be an operational product providing water vapor density data every 5 min (the one set in this article according to the reference humidity sensor resolution, or other time steps can be set according to the actual situation). The results show that the inverted water vapor density obtained by the model is in good agreement with that calculated from humidity and temperature sensor measurements. In addition, the water vapor density inversion model based on GRU is compared with that based on LSTM.

As E-band CMLs (as part of the new 5G network) are widely distributed in urban areas, meteorological information monitoring technology based on CMLs will present new development

opportunities. Compared with previous CMLs operating in the range of 10 to 40 GHz, E-band CMLs are more sensitive to meteorological elements such as the rain rate, raindrop size distribution, and water vapor [34]. With continuous improvements in the reconstruction technology of different meteorological fields based on CMLs in the future, these instruments are expected to provide indispensable support for global weather monitoring.

ACKNOWLEDGMENT

The authors would like to thank Martin Fencl for the open-source data.

REFERENCES

[1] G. S. Benton, R. T. Blackburn, and V. O. Snead, "The role of the atmosphere in the hydrologic cycle," *EOS, Trans. Amer. Geophys. Union*, vol. 31, no. 1, pp. 61–93, 1950.
[2] B. Lennart, "The global atmospheric water cycle," *Environ. Res. Lett.*, vol. 5, no. 2, 2010, Art. no. 025202.
[3] R. Philipona, D. Bruno, A. Ohmura, and C. Ruckstuhl, "Anthropogenic greenhouse forcing and strong water vapor feedback increase temperature in Europe," *Geophys. Res. Lett.*, vol. 32, no. 19, 2005, Art. no. L19809.
[4] J. C. Brimelow and G. W. Reuter, "Transport of atmospheric moisture during three extreme rainfall events over the mackenzie river basin," *J. Hydrometeorol.*, vol. 6, no. 4, pp. 423–440, 2005.
[5] M. Gustafsson, D. Rayner, and D. Chen, "Extreme rainfall events in southern Sweden: Where does the moisture come from?," *Tellus Ser. A-Dyn. Meteorol. Oceanogr.*, vol. 62, no. 5, pp. 605–616, 2010.
[6] K. E. Trenberth, "Atmospheric moisture recycling: Role of advection and local evaporation," *J. Climate*, vol. 12, no. 5, pp. 1368–1381, 1999.
[7] K. Emanuel, D. Raymond, A. Betts, L. Bosart, and A. Thorpe, "Report of the first prospectus development team of the U.S. weather research program to NOAA and the NSF," *Bull. Amer. Meteorol. Soc.*, vol. 76, pp. 1194–1208, 1995.
[8] A. D. D. Genio, "The dust settles on water vapor feedback," *Science*, vol. 296, no. 5568, pp. 665–666, 2002.
[9] S. Solomon *et al.*, "Contributions of stratospheric water vapor to decadal changes in the rate of global warming," *Science*, vol. 327, no. 5970, pp. 1219–1223, 2010.
[10] Z. M. Rittersma, A. Splinter, A. Bödecker, and W. Benecke, "A novel surface-micromachined capacitive porous silicon humidity sensor," *Sensors Actuators B: Chem.*, vol. 68, no. 1–3, pp. 210–217, 2000.
[11] Y. Luo, Y. Kun, Y. Shi, and C. Shang, "Research of radiosonde humidity sensor with temperature compensation function and experimental verification," *Sensors Actuators A: Phys.*, vol. 218, pp. 49–59, 2014.
[12] T. J. Kleespies and L. M. McMillin, "Retrieval of precipitable water from observations in the split window over varying surface temperatures," *J. Appl. Meteorol.*, vol. 29, no. 9, pp. 851–862, 1990.
[13] L. Gu, Q. A. Huang, and M. Qin, "A novel capacitive-type humidity sensor using CMOS fabrication technology," *Sensors Actuators B: Chem.*, vol. 99, no. 2–3, pp. 491–498, 2004.
[14] K. E. Cady-Pereira, M. W. Shephard, D. D. Turner, E. J. Mlawer, S. A. Clough, and T. J. Wagner, "Improved daytime column-integrated precipitable water vapor from Vaisala radiosonde humidity sensors," *J. Atmos. Ocean. Technol.*, vol. 25, no. 6, pp. 873–883, 2008.
[15] G. J. Jedlovec, "Precipitable water estimation from high-resolution split window radiance measurements," *J. Appl. Meteorol.*, vol. 29, no. 9, pp. 863–877, 1990.
[16] J. C. Liljegren, E. E. Clothiaux, G. G. Mace, S. Kato, and X. Dong, "A new retrieval for cloud liquid water path using a ground-based microwave radiometer and measurements of cloud temperature," *J. Geophys. Res.: Atmos.*, vol. 106, no. D13, pp. 14485–14500, 2001.
[17] P. Alpert, H. Messer, and N. David, "Mobile networks aid weather monitoring," *Nature*, vol. 537, no. 7622, pp. 617–617, 2016.
[18] N. Davıd and H. O. Gao, "Atmospheric monitoring using commercial microwave networks," in *Proc. 15th Int. Conf. Environ. Sci. Technol.*, 2017.
[19] K. Song, X. Liu, T. Gao, M. Yin, and B. He, "The feasibility analysis of cellphone signal to detect the rain: Experimental study," *IEEE Geosci. Remote Sens. Lett.*, vol. 17, no. 7, pp. 1158–1162, Jul. 2020.
[20] C. Chwala and H. Kunstmann, "Commercial microwave link networks for rainfall observation: Assessment of the current status and future challenges," *Wiley Interdiscipl. Rev., Water*, vol. 6, no. 2, 2019, Art. no. e1337.
[21] H. Messer, A. Zinevich, and P. Alpert, "Environmental monitoring by wireless communication networks," *Science*, vol. 312, no. 5774, May 2006, Art. no. 713.
[22] H. Minda and K. Nakamura, "High temporal resolution path-average rain gauge with 50-GHz band microwave," *J. Atmos. Ocean. Technol.*, vol. 22, no. 2, pp. 165–179, 2005.
[23] A. Overeem, H. Leijnse, and R. Uijlenhoet, "Measuring urban rainfall using microwave links from commercial cellular communication networks," *Water Resour. Res.*, vol. 47, no. 12, p. W12505, 2011.
[24] O. Goldshtein, H. Messer, and A. Zinevich, "Rain rate estimation using measurements from commercial telecommunications links," *IEEE Trans. Signal Process.*, vol. 57, no. 4, pp. 1616–1625, Apr. 2009.
[25] K. Song, X. Liu, T. Gao, and B. He, "Raindrop size distribution retrieval using joint dual-frequency and dual-polarization microwave links," *Adv. Meteorol.*, vol. 2019, pp. 1–11, 2019.
[26] T. C. van Leth, H. Leijnse, A. Overeem, and R. Uijlenhoet, "Estimating raindrop size distributions using microwave link measurements: Potential and limitations," *Atmos. Meas. Techn.*, vol. 13, no. 4, pp. 1797–1815, 2020.
[27] K. Pu, X. Liu, M. Xian, and T. Gao, "Machine learning classification of rainfall types based on the differential attenuation of multiple frequency microwave links," *IEEE Trans. Geosci. Remote Sens.*, vol. 58, no. 10, pp. 2158–2170, Oct. 2020.
[28] K. Pu, X. Liu, S. Hu, and T. Gao, "Hydrometeor identification using multiple-frequency microwave links: A numerical simulation," *Remote Sens.*, vol. 12, no. 13, pp. 2158–2179, 2020.
[29] N. David, O. Sendik, H. Messer, and P. Alpert, "Cellular network infrastructure: The future of fog monitoring?," *Bull. Amer. Meteorol. Soc.*, vol. 96, no. 10, pp. 1687–1698, 2015.
[30] N. David and H. O. Gao, "Using cellular communication networks to detect air pollution," *Environ. Sci. Technol.*, vol. 50, no. 17, pp. 9442–9451, 2016.
[31] N. David, P. Alpert, and H. Messer, "Technical note novel method for water vapour monitoring using wireless communication networks measurements," *Atmos. Chem. Phys.*, vol. 9, no. 7, pp. 2413–2418, 2009.
[32] N. David *et al.*, "Analyzing the ability to reconstruct the moisture field using commercial microwave network data," *Atmos. Res.*, vol. 219, pp. 213–222, 2019.
[33] B. Ji, Y. Li, S. Chen, C. Han, C. Li, and H. Wen, "Secrecy outage analysis of UAV assisted relay and antenna selection for cognitive network under Nakagami-m channel," *IEEE Trans. Cogn. Commun. Netw.*, vol. 6, no. 3, pp. 904–914, Sep. 2020.
[34] M. Fencl, M. Dohnal, P. Valtr, M. Grabner, and V. Bareš, "Atmospheric observations with E-band microwave links—Challenges and opportunities," *Amtos. Meas. Techn.*, vol. 13, pp. 6559–6578, 2020.
[35] A. L. Buck, "New equations for computing vapor pressure and enhancement factor," *J. Appl. Meteorol. Climatol.*, vol. 20, no. 12, pp. 1527–1532, 1981.
[36] J. J. Hopfield, "Neural networks and physical systems with emergent collective computational abilities," *Proc. Nat. Acad. Sci. United States Amer.*, vol. 79, no. 8, pp. 2554–2558, 1982.
[37] S. Fernández, A. Graves, and J. A. Schmidhuber, "An application of recurrent neural networks to discriminative keyword spotting," in *Proc. Int. Conf. Artif. Neural Netw.*, 2007, pp. 220–229.
[38] S. Haykin, *Neural Networks and Learning Machines Third Edition*. New York, NY, USA: Pearson Education, 2009.
[39] S. Hochreiter and J. Schmidhuber, "Long short-term memory," *Neural Comput.*, vol. 9, no. 8, pp. 1735–1780, 1997.
[40] K. Cho, B. V. Merriënboer, D. Bahdanau, and Y. Bengio, "On the properties of neural machine translation: Encoder-decoder approaches," *Comput. Sci.*, vol. 2, pp. 103–111, 2014.

Kang Pu received the master's degree in atmospheric sciences from National University of Defense Technology, Nanjing, China, in 2020. He is currently working toward the doctoral degree in atmospheric measurement techniques at the College of Meteorology and Oceanography, National University of Defense Technology, Changsha, China.

His research interests include atmospheric measurement and remote sensing techniques and instruments.

Xichuan Liu received the master's degree in atmospheric measurement techniques from PLA University of Science and Technology, Nanjing, China, in 2010, and the Ph.D. degree in atmospheric measurement techniques from PLA University of Science and Technology, Nanjing, China, in 2014.

He is currently an Associate Professor with the College of Meteorology and Oceanography, National University of Defense Technology, Changsha, China. His research interests include atmospheric physics, atmospheric measurement, and remote sensing techniques and instruments.

Lei Liu received the master's degree in atmospheric physics and atmospheric environment from PLA University of Science and Technology, Nanjing, China, in 2008, and the Ph.D. degree in atmospheric physics and atmospheric environment from PLA University of Science and Technology, Nanjing, China, in 2015.

He is currently an Associate Professor with the College of Meteorology and Oceanography, National University of Defense Technology, Changsha, China. His research interests include radiative transfer model, atmospheric measurement, and remote sensing techniques and instruments.

Taichang Gao received the B.S. degree in dynamic meteorology from the Air Force College of Meteorology, Nanjing, China, in 1982.

He is currently a Professor with the College of Meteorology and Oceanography, National University of Defense Technology, Nanjing, China. His research interests include atmospheric measurement and remote sensing techniques and instruments.